Geophys. J. Int. (2006) **167,** 1353–1362 doi: 10.1111/j.1365-246X.2006.03124.x

Signal restoration through deconvolution applied to deep mantle seismic probes

W. Stefan,[1] E. Garnero[2] and R. A. Renaut[1]

[1]*Department of Mathematics and Statistics, Arizona State University, Temple AZ, 85287-1804 USA. E-mail: stefan@mathpost.la.asu.edu*
[2]*Department of Geological Science, Arizona State University, Temple AZ, 85287-1804 USA*

Accepted 2006 July 3. Received 2006 June 30; in original form 2005 March 26

SUMMARY

We present a method of signal restoration to improve the signal-to-noise ratio, sharpen seismic arrival onset, and act as an empirical source deconvolution of specific seismic arrivals. Observed time-series g_i are modelled as a convolution of a simpler time-series f_i, and an invariant point spread function (PSF) h that attempts to account for the earthquake source process. The method is used on the shear wave time window containing *SKS* and *S*, whereby using a Gaussian PSF produces more impulsive, narrower, signals in the wave train. The resulting restored time-series facilitates more accurate and objective relative traveltime estimation of the individual seismic arrivals. We demonstrate the accuracy of the reconstruction method on synthetic seismograms generated by the reflectivity method. Clean and sharp reconstructions are obtained with real data, even for signals with relatively high noise content. Reconstructed signals are simpler, more impulsive, and narrower, which allows highlighting of some details of arrivals that are not readily apparent in raw waveforms. In particular, phases nearly coincident in time can be separately identified after processing. This is demonstrated for two seismic wave pairs used to probe deep mantle and core–mantle boundary structure: (1) the S_{ab} and S_{cd} arrivals, which travel above and within, respectively, a 200–300-km-thick, higher than average shear wave velocity layer at the base of the mantle, observable in the 88–92 deg epicentral distance range and (2) *SKS* and SP_{diff} *KS*, which are core waves with the latter having short arcs of *P*-wave diffraction, and are nearly identical in timing near 108–110 deg in distance. A Java/Matlab algorithm was developed for the signal restoration, which can be downloaded from the authors web page, along with example data and synthetic seismograms.

Key words: core–mantle boundary, D″, deconvolution, lower mantle, regularization, total variation.

1 INTRODUCTION

Nearly all of the Earth's interior remains inaccessible, thus remote sampling of the interior is required. Presently, seismic waves provide the most detailed view of the interior's elastic structure. Seismic determination of Earth structure involves, for example,

(a) accurate characterization of seismic energy that has sampled the interior (depth and geography) of interest,
(b) reliable estimation or measurement of seismic wave timing, amplitude, and frequency content and
(c) realistic reproduction of observed wave attributes, such as time or waveform predictions from computational methods.

An important challenge is the requirement of clean and impulsive seismic energy with good signal-to-noise ratio (SNR). A variety of factors, however, result in greatly reduced numbers of usable data due to high noise levels. Thus any method that aids in denoising time-series data stands to greatly benefit studies of the Earth as a system.

Traveltime and waveform measurements play an important role in characterizing the Earth's deep interior, in both the tomographic inversion approach (e.g. Bijwaard *et al.* 1998; Masters *et al.* 2000; Boschi & Dziewonski 2000; Kárason & van der Hilst 2001; Gu *et al.* 2001; Grand 2002; Ritsema & van Helst 2000) as well as forward analyses (e.g. Wysession *et al.* 1999; Garnero 2000; Ni *et al.* 2002; Rost & Revenaugh 2001; Ni & Helmberger 2003; Castle & van der Hilst 2003). However, each earthquake has its own frequency and source-time evolution behaviour, and recording stations vary in their site conditions and instrument type, thus earthquake source and SNRs often vary significantly in any given data set. Signals can be averaged (stacked) to construct empirical source shapes for deconvolution in the time domain (as in Lay *et al.* 2004), though this typically introduces Gibbs phenomena, and does not address station noise. The methods pursued here seek improved timing measurements, whether made by hand or by cross-correlation with some reference pulses such as synthetic seismograms or an estimate of the earthquake source time mechanism. Methods that facilitate more accurate timing measurements of signals in the presence of noise stand to increase the quantity (and quality) of data that can be used for Earth structure studies. This includes the study of geographical regions of interest that are limited because sparse earthquake seismicity often results in less data with adequate SNR. Seismic array methods have been shown to significantly enhance SNRs (Rost & Thomas 2004). The current geographical distribution of traditional seismic arrays is, however, limited in comparison to that of stand along threee-component seismometers. Thus, improving the quality of individual seismogram data holds promise for improving Earth structure interrogation.

In this study we address removal of source, receiver structure, and the noise in the signal, leaving only the part of the signal most directly due to reflecting surfaces and heterogeneities. Our technique effectively sharpens seismic signal Onsets, and improves the visibility of the emergence of secondary seismic arrivals from a dominant reference phase. We focus our approach on the application of differential seismic wave analyses, as most deep Earth studies reference one seismic arrival to another (e.g. Garnero 2000). We first present the method, which is a convolution-based approach with total variation (TV) regularization (Rudin *et al.* 1992). We then demonstrate and validate the method on two different examples: (1) signal restoration of *SKS* and *S* (or $S_{\rm diff}$) in synthetic seismograms and (2) the restoration of actual data for 31 seismic recordings of a deep focus South American earthquake. We show how deconvolved seismograms can be automatically measured for relative traveltime determination and for waveform distortion diagnostics. We also demonstrate the method's utility for detection of two very similar shaped pulses that are nearly superposed in time, which in raw data appear as a broadening or deformation of the dominant phase. The software used to deblur the signals and all examples are available (Stefan *et al.* 2005).

2 MATHEMATICAL MODEL

In many applications, such as traveltime inversion tomography (e.g. VanDecar 1991), accurate measurement of the arrival time of seismic phases is very important. However, robust measurement of the traveltimes is often difficult, particularly when data lacks clearly defined onsets. Traveltime determination by hand is challenging because background noise often obscures confident identification of signal initiation. Cross-correlation between the signal of interest and a reference phase depends on the similarity of the two phases. This condition is not always met, due to, for example, differential attenuation or one phase being altered from scattering, multipathing, or anisotropy.

In the approach presented here, we apply a pre-processing of the signal, which is designed to sharpen signal onsets such that the process of determining arrival times is more robust. Our approach inherently accounts for waveform similarity across a suite of recordings (e.g. a given seismic arrival across all stations recording a given earthquake), thus enabling more reliable relative traveltime estimation of phase initiation.

2.1 Signal degradation

We assume the recorded signal g is the composition of the source signal (S), blurring effects of the Earth such as attenuation (A) and scattering heterogeneities (H) and path effects (P) that include geometric spreading, reflection from internal interfaces (and so on), and additive noise (N), and that we can model these effects by a convolution

$$g = S * A * H * P + N,$$

where we try to reconstruct the part of the signal that contains the path effects. We cannot expect to reconstruct the signal exactly because the source and attenuation are usually unknown. Hence, we will call the approximated desired signal f and the approximation of the combination of source and attenuation h, that is, we assume that the observed signal g (e.g. the time-series containing *SKS* and *S*) is the result of the convolution of the sharp signal f and the point spread function (PSF) h, plus the addition of noise n (Claerbout 1985; Clayton & Wiggins 1976; Vogel 2002),

$$g = f * h + n, \tag{1}$$

here $*$ is the discrete convolution operator for two vectors f and h,

$$(f * h)_k = \sum_i f_i h_{k-i+1}.$$

For example, a convolution with a Gaussian

$$h(t) = \frac{1}{\sigma\sqrt{2\pi}} e^{-\frac{t^2}{2\sigma^2}}, \tag{2}$$

where the parameter σ governs the width of the function, results in a σ-dependent blurring of the input signal. Fig. 1 illustrates two examples of the impact of PSFs on a given signal.

2.2 Signal restoration withoutregularization

The goal of the signal restoration process is to identify the original signal f in eq. (1), given the observed signal g. A direct approach,

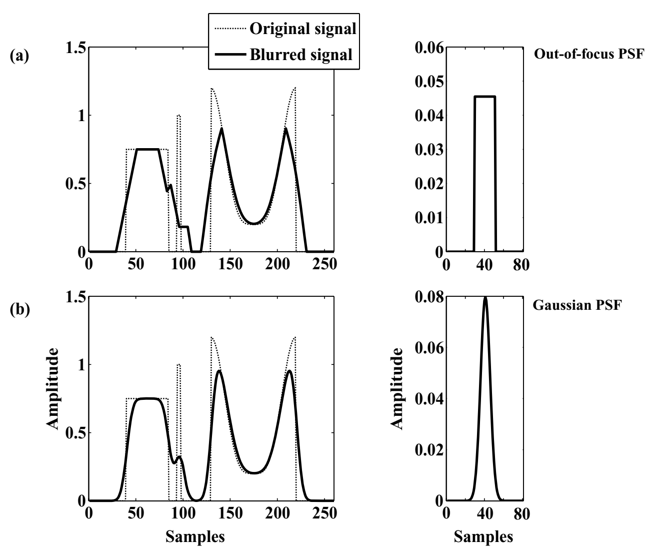

Figure 1. Examples of blurring by different PSFs. In both panels the left picture shows a test signal (dashed line) and the blurred test signal (solid line) blurred by a PSF (right-hand side picture) using the convolution-based operator (1), where f is the test signal, h is the PSF and g is the resulting blurred signal. No noise was added (i.e. $n \equiv 0$) and h is normalized, $\sum h_i = 1$, to preserve the amplitude of the unblurred signal in the blurred signal. Panel (a) shows blurring by an out-of-focus PSF. This kind of PSF models out of focus lenses in 2-D and is constant on a disk. In the 1-D case it is constant on an interval. It transforms all sharp onsets and offsets in a line with constant slope, and smoothes out the small impulse in the test signal. Panel (b) shows the blurring resulting from a Gaussian PSF (2). It blurs the onsets in a smoother way and also smoothes out the small impulse.

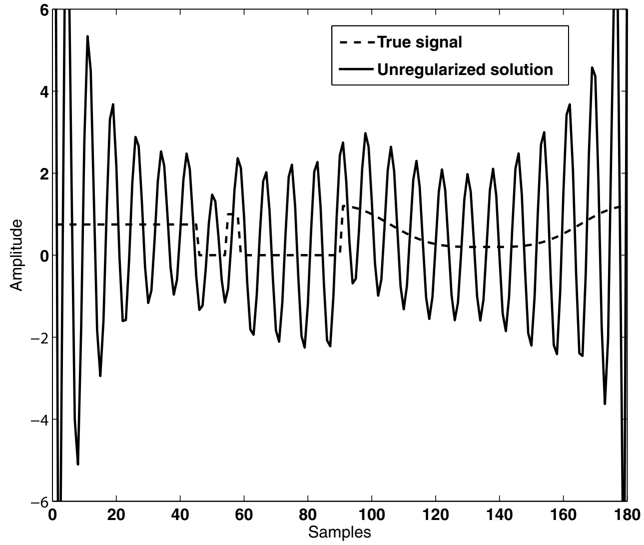

Figure 2. Result of unregularized deconvolution of a test signal. The test signal f (dashed line) was blurred by the operator in (1) using a Gaussian PSF and additive white noise with an amplitude of 0.01 added to the blurred signal. The picture illustrates a significant amplification of the noise through the reconstruction. The amount of noise amplification depends on the choice of the PSF.

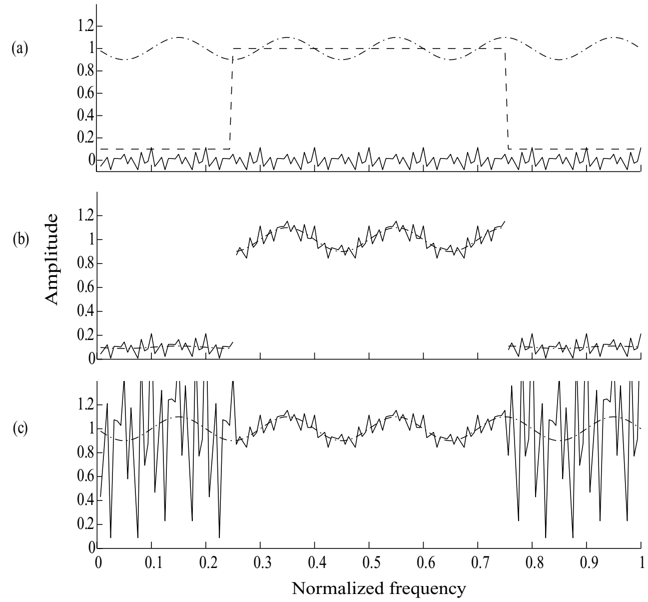

Figure 3. Schematic illustration of the ill-posedness of the deconvolution problem. (a) Shows a test signal in frequency domain (dashed-dotted line), the PSF of a band pass filter in frequency domain (dashed line) with height of 0.1 on the left- and right-hand side and 1 in the middle part. The solid line shows an additive noise component. (b) Shows the band pass filtered (convolved) test signal with and without noise. In the frequency domain this signal is obtained by point wise multiplication of the original signal and the PSF, that is, the left and right-hand side portions of the original signal are multiplied by 1/10. The noise is added to the filtered signal. (c) Shows the deconvolved signal without and with noise. In the frequency domain the unregularized deconvolution is done by point wise dividing by the PSF (i.e. here multiplying the left-hand side and the right-hand side portions of the signal by 10). This process not only amplifies the signal but also the noise, resulting in the high noise content in the reconstruction.

given h, is to find an approximation $\hat{f}$ to f which minimizes the error in the fit to the data through minimization of the norm of the residual r

$$\hat{f} = \arg\min_f \|r\|_2^2 = \arg\min_f \|g - f * h\|_2^2, \tag{3}$$

where arg min denotes the argument that minimizes the expression in the brackets. For noisy data, however, this does not result in a usable reconstruction due to the associated very high amplification of any noise in the signal. Fig. 2 shows that the additive noise of amplitude 0.01 is amplified to an amplitude of about 2–10, that is, by a factor of 200–1000. The amplification arises because of the extreme ill-posedness of the deconvolution problem (Andrews & Hunt 1977; Katsaggelos 1991; Bertero & Boccacci 1998; Vogel 2002). For example, suppose that we attempt to reconstruct the original unfiltered signal from an observed signal which has already been filtered by a band pass filter. Fig. 3 illustrates the effects of the ill-posedness: small changes in the input result in large changes in the output. In particular this means that unavoidable small changes from noise contamination are amplified.

In order to obtain a low noise solution we have to provide additional information about the smoothness of the function. This results in a regularized (Bertero & Boccacci 1998) problem. In practice, this is done by adding a regularization term which penalizes signals with high noise (Vogel 2002).

2.3 Signal restoration with regularization

Including regularization in eq. (3) yields the problem

$$\hat{f} = \arg\min_f \left\{\|r\|_2^2 + \lambda R(f)\right\}, \tag{4}$$

in which the second term $R(f)$ is the regularization term. The parameter λ governs the trade-off between the fit to the data and the smoothness of the reconstruction. Two common regularization methods based on penalizing the noise by an estimate based on the derivative of f are Tikhonov and TV regularization (Vogel 2002). These choices yield results with different characteristic shapes; regularization using TV yields a piecewise constant reconstruction (Ring 1999) and preserves the edges of the signal, while Tikhonov yields a smooth reconstruction, see Fig. 4. The norm for r in all cases is L_2; other methods with L_1 residual can be found for example in Claerbout & Muir (1973) and Claerbout (1985). This method can be applied to each individual signal, as compared to a least squares fit, which operates on a stack of signals (Claerbout *et al.* 1973), which is important in the case of sparse data coverage. A compilation of solutions using different regularization techniques including a variation of the method in Claerbout *et al.* (1973) (with L_2 residual), the Wiener deconvolution (Margrave 2001) and Water level deconvolution (Clayton & Wiggins 1976) can be found in Fig. 5. All methods resolve the peak next to *SKS* for an exactly known PSF in panel (a). The Wiener deconvolution results in a reconstruction of multiple peaks, that is, produces artefacts since the minimum phase assumption required for the Wiener deconvolution is violated. L_1 regularization shows a very clear result (one large delta impulse at the position of *SKS* and a smaller one at the position of *SPdKS*) for the exactly known PSF and fails for an approximated PSF in Panel (b). The TV solution shows in both cases a consistent indication of *SPdKS* without introducing additional artefacts. The success or failure of the different regularization techniques depends on assumptions about the signal to be reconstructed. In case of TV we assume a signal with sparse jump discontinuities, that is, a piecewise constant

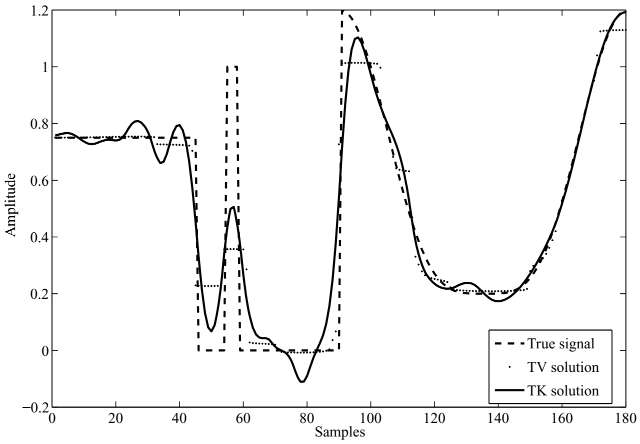

Figure 4. Regularized deconvolution: The dashed line shows the original test signal. The test signal was blurred using the forward model (1) and the out-of-focus blur in Fig. 1. The solid line shows the Tikhonov regularized solution is smooth in the curved parts of the signal but the jumps in the signal are still blurred and Gibb's phenomena are introduced near the edges. The dotted line shows the TV regularized method results in a piecewise constant reconstruction and the position of the edges are preserved. This result also illustrates, however, the typical loss in contrast of TV, that is, the ratio between low and high point of the peak is reduced. In both cases the peak in the middle can only be partially reconstructed because some of the information of the original signal is lost in the noise after the blurring.

signal. Methods like Wiener deconvolution assume a signal that is a realization of white noise.

For our application we are interested in a sharp reconstruction of the seismic signals and, therefore, TV is the best choice. The TV of a function f as defined by Rudin *et al.* (1992)

$$\mathrm{TV}(f) = \int_{-\infty}^{\infty} |f'(t)|\, dt, \tag{5}$$

is non-differentiable. We thus use

$$\mathrm{TV}_\beta(f) = \int_{-\infty}^{\infty} \sqrt{f'(t)^2 + \beta}\, dt, \tag{6}$$

where $\beta > 0$ is small (Vogel 2002). The resulting reconstruction is no longer piecewise constant but has round edges, see Fig. 6. A larger β results in a smoother objective function in eq. (4) and thus a faster converging minimization. Although the edges of the signal are still visible, it is also clear that the extent of the smoothing depends on the size of β.

For the rest of this paper we assume that the signal degradation, that is, the blurring of the true signal can be modelled by a Gaussian PSF (eq. 2) with width parameter σ. The choice of σ is subjective; for this application, we empirically choose a σ which yields the sharpest reconstruction of the signal, that is, the one that results in the sharpest onsets of the seismic arrivals of interest. Small σ correspond to less deblurring while a too large σ will result in unwanted oscillations. The penalty parameter λ in eq. (4) can be chosen by the

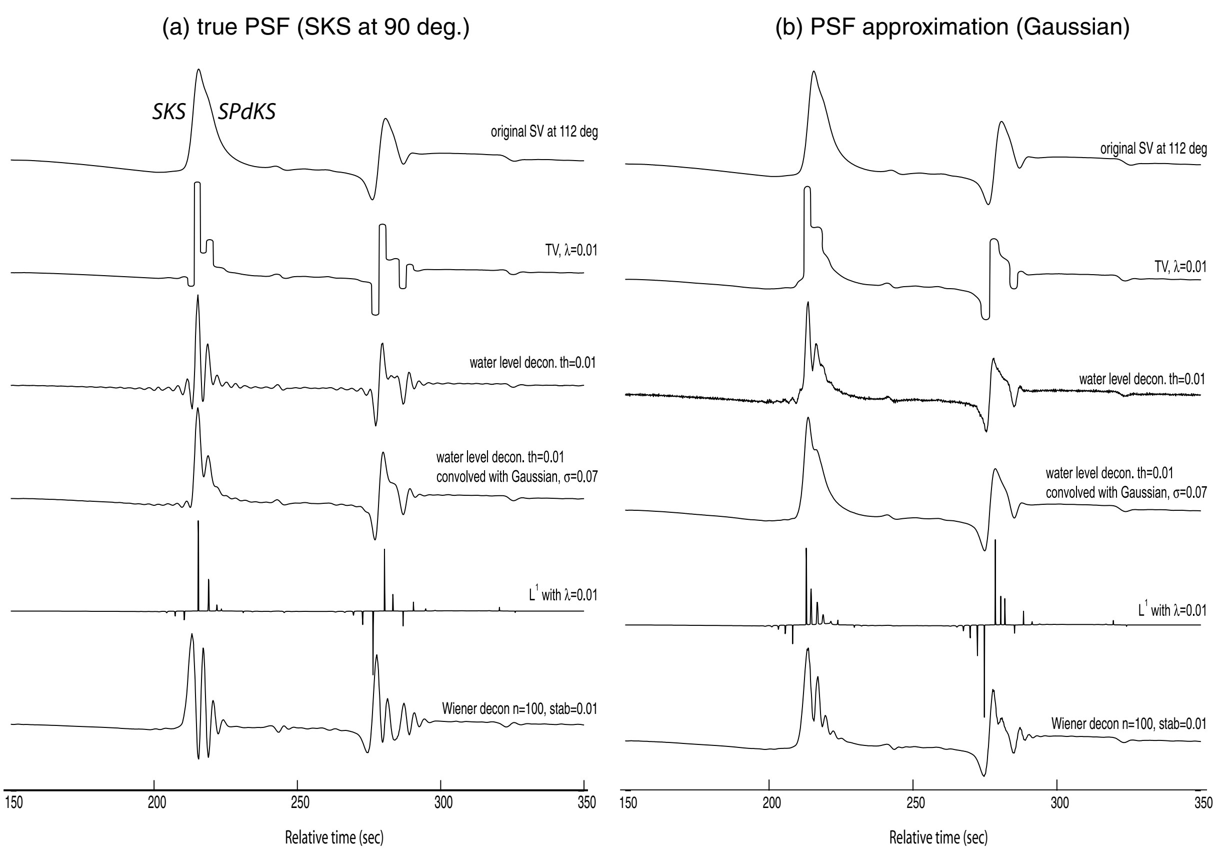

Figure 5. Regularized deconvolution of synthetic SV displacement data. Panel (a) shows the separation of *SKS* and *SPdKS* by the deconvolution using the exact PSF of a synthetic SV trace at 112 deg. for which *SPdKS* occurs about 5 s after *SKS*. The goal of the deconvolution is to separate *SKS* from *SPdKS*. Panel (b) shows the more practical case of an unknown, thus only approximated PSF. TV shows in both cases clear evidence of *SPdKS* in the form of a second peak in (a) and a broadening of *SKS* in (b).

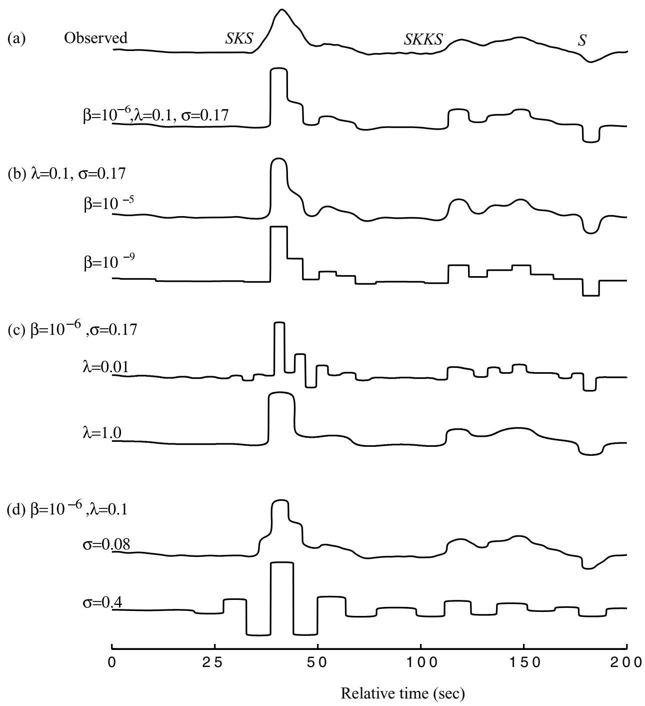

Figure 6. This figure shows the effect of different choices of β, λ and σ. (a) Shows the SV displacement data of an event in South America on 2000 May 12 with $M_b = 7.2$ at a depth of 225 km picked up at the station in Moni Apezanon in Crete at a epicentral distance of 104.1 deg. The *SKS* amplitude is normalized to unit. (b) Shows the effect of a different β where λ and σ is fixed. (c) The effect of a different λ and (d) the effect of a different σ.

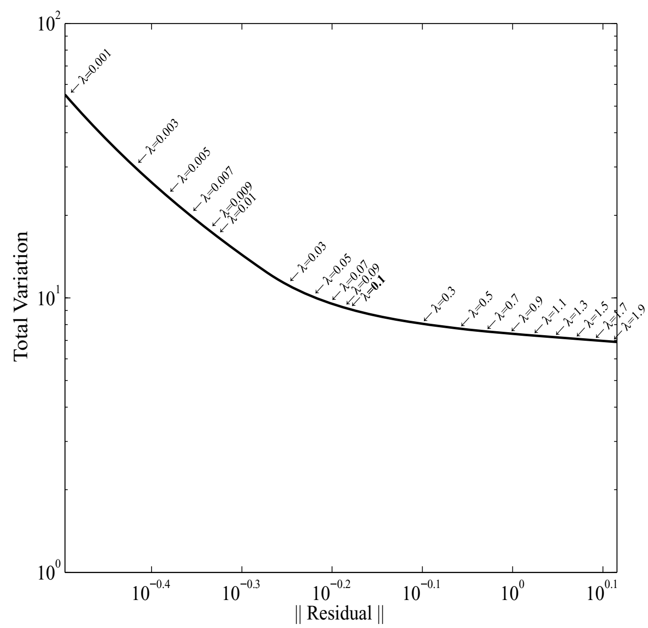

Figure 7. L-curve: This plot shows the trade-off between the smoothness and the data fit. The *x*-axis shows the norm of the residual, that is, the measure of how well the reconstruction fits the given data. The *y*-axis shows the regularization term, that is, the smoothness measurement (here TV). The graph shows that a better data fit leads to a less smooth reconstruction. The parameter λ can be used to govern this trade off. For each choice of λ there is a corresponding point on the L-curve (here indicated by the arrow and the corresponding value of λ). Usually the graph has a corner point thus the name L-curve. The corner point is usually chosen as the point which gives the best trade-off in these errors. The reconstructions in Fig. 6 show the reconstruction with different λ.

L-curve approach, (Hansen 1994), in which the smoothness measurement (i.e. the regularization term, here the TV) and the data-fit measurement are plotted on an *x–y* plot. Fig. 7 shows the L-curve for the test case in Fig. 6. When λ is too large, the small-scale structures of the signal are removed through oversmoothing of the signal. Choosing λ too small results in a high noise content in the reconstruction. The effect of different choices of parameters is illustrated in Fig. 6.

While TV-based denoising and TV-regularized deconvolution have successfully been applied in many applications for a variety of signals, including medical and astronomical imaging (Vogel & Oman 1996; Jonsson *et al.* 1998; Keeling 2002), it does not appear to have been adopted specifically for edge detection as proposed in this report. TV regularization results in virtually noise-free reconstructions (i.e. excellent reconstructed signal to background noise levels) of piecewise constant functions, and is known to preserve the position of edges (Ring 1999; Strong & Chan 2000). Moreover, in relevant applications, namely those which are very ill-posed and noise contaminated, it yields very robust reconstructions. As we will show in the examples in Section 3, this is also the case for seismic signals.

2.4 Numerical formulation

The proposed method of signal restoration requires an efficient algorithm which minimizes the objective function

$$J(f) = \|g - f * h\|_2^2 + \lambda \mathrm{TV}_\beta(f). \quad (7)$$

The necessary steps in the calculation of the objective function, and its minimization by the limited memory BFGS (L-BFGS) method (Zhu *et al.* 1997; Nocedal & Wright 1999), are described in an electronic supplement. The edge detection applied to the deconvolved signals is also presented in the electronic supplement (Stefan *et al.* 2005).

3 EXPERIMENTS

We demonstrate the deconvolution method with the edge detection on synthetic and real seismic data.

3.1 Synthetic seismograms

First we look at synthetic seismograms produced using the 1-D PREM reference model (Dziewonski & Anderson 1981). The synthetic seismograms were generated by the reflectivity method (Müller 1985) for an earthquake at a depth of 500 km. Receiver distances are from 90 to 115 degrees, in 1 degree increments. Fig. 8 shows *SKS* at 90 degrees, which illustrates how the deconvolution process transforms the original seismic signal into a much sharper signal, without introducing additional noise or artefacts. The usage of a centred PSF results in a reconstruction that is centred around the maximum of *SKS*. This means, however, that the arrival time of *SKS* in the reconstruction is shifted compared to the arrival time of *SKS* in the original record. While absolute traveltime information can be retrieved by methods that approximate the half width of the PSF, in this paper we focus on relative timing and waveshape information between a given seismic phase at different seismographic stations, as well as two different arrivals at a single station.

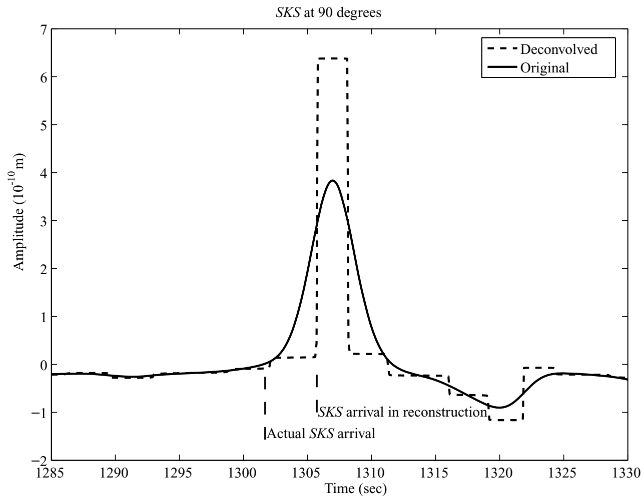

Figure 8. Deconvolution of a synthetic *SKS* at 90 degrees. The synthetic SV wave train was deconvolved using a Gaussian PSF with $\sigma = 0.12$, sampled from $-1/2$ to 1/2 at 256 points by minimizing (7) with $\lambda = .01$ using the L-BFGS algorithm described in an electronic supplement. The deconvolution transforms the original *SKS* phase (solid line) into a sharp rectangle, where it is very easy to see the onset time of *SKS*.

Fig. 9 shows a time–distance plot of the original and deconvolved synthetic *SV* wave trains aligned at the *SKS* arrival time obtained after employing the edge detection method on the deconvolved signals. The development and subsequent move out of $SP_{\text{diff}}KS$ relative to *SKS* is seen at the larger distances (i.e. >108 deg). This process is more pronounced in the deconvolved traces than in the original seismograms, and presents a clear advantage over traditional methods for studying core–mantle boundary structure, e.g. ultra-low velocity zones (ULVZ), with $SP_{\text{diff}}KS$ (e.g. see Thorne & Garnero 2004).

Finally, to assess the accuracy of the time measurements we consider the difference of our estimates of the differential time of *SKS* and *S* arrivals from the deconvolved synthetics to those by ray theory for the PREM model. This measurement is independent of the earlier described shifting effect. Fig. 10 shows that the prediction agrees reasonably well at distances less than 105 deg (roughly less than ± 0.2 s difference). Between the distances of 105 and 112 deg, *SPdKS* initiates, causing *SKS* to broaden, and thus has an altered frequency content. This slightly degrades the predictions from our method. A similar phenomenon occurs beyond 112 deg, where the *S* wave is well into diffraction around the core, and ray theory is inappropriate. However, these errors are relatively small compared to those introduced from measurements by hand or by cross-correlation with a master pulse, each of which can yield much higher errors (± 1.0 s, e.g. see Moore *et al.* 2004). Fig. 10 also shows that our approach is not very sensitive to the reconstruction parameters. In particular, the figure shows that the measurement error is almost the

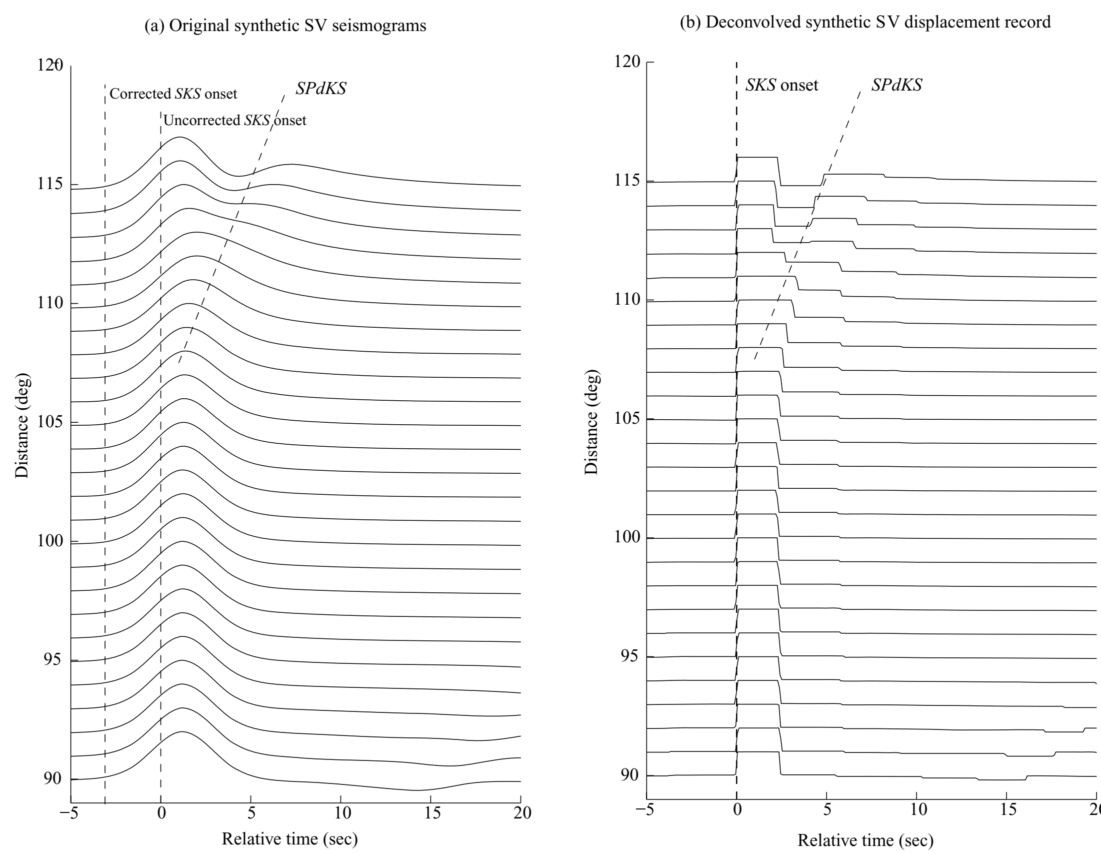

Figure 9. (a) SV component reflectivity synthetics, for a source depth of 500 km. Receiver distances are from 90 to 115 degrees, in one degree increments. Sampling rate is 0.1 s, $\lambda = 0.01$, $\sigma_{SV} = 0.12$, and $\beta = 10^{-6}$. (b) Deconvolved synthetics. Traces in both panels are aligned at the detected *SKS* onset in panel (b) using an edge detection method. At a distance of 108 deg, the formation and subsequent move out of $SP_{\text{diff}}KS$ can be seen in both plots, though it is first visible in the deconvolved traces: *SKS* remains rectangular until the formation of $SP_{\text{diff}}KS$ initiates, which first broadens *SKS*, and then emerges as an additional rectangle.

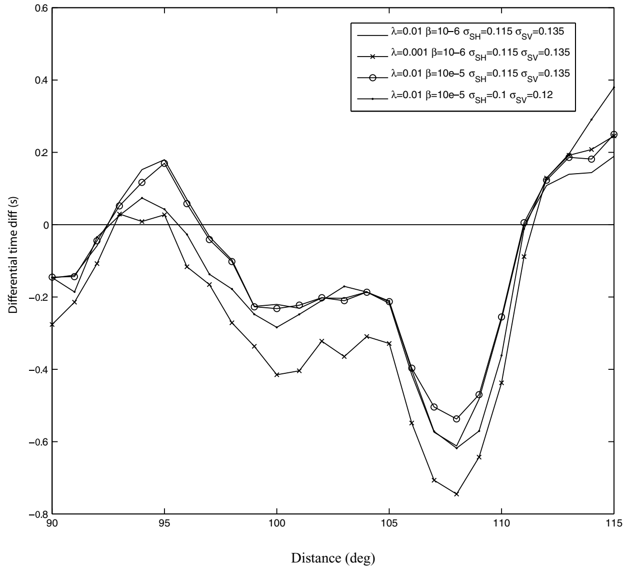

Figure 10. The difference between S minus *SKS* differential traveltimes ($T_{S\text{–}SKS}$): plotted are $T_{S\text{–}SKS}$ computed from our method applied to reflectivity synthetic seismograms subtracted from those measured by ray theory, both for the PREM model. This difference is compared for several restoration parameter choices.

same for $\beta = 10^{-6}$ and $\beta = 10^{-5}$, σ and λ have a bigger impact, though traveltimes stay within roughly 0.1 s of the other parameter choices.

3.2 Real seismic data

In the following we apply our method to the records of an earthquake in South America $M_b = 7.2$ on 2000 May 12, recorded at 31 broadband stations in Europe.

Fig. 11 shows a compilation of different regularization techniques applied to this signal. The results compare very well to the synthetic case in Fig. 5. The indication of *SPdKS* in the form of a broadening of *SKS* in the TV solution is very similar to the synthetic case. Also TV seems to handle the noise in the signal, in particular before the *SKS* arrival, much better than the other methods. The L_1 solution has the same problem as in the Fig. 5 panel (b), namely it shows multiple delta impulses instead of a single one at the location of *SPdKS*. Fig. 12 shows the original and deconvolved *SH* and *SV* traces in distance profiles. Thus the sharp rectangular pulse shape that was obtained in the synthetic seismograms is also obtained for real data. Moreover, the deconvolved data facilitates possible detection of nearly overlapping phases (here S_{ab} and S_{cd}). This is further emphasized in Fig. 13, in which the SH traces of Fig. 12 are grouped into distance bins and then stacked. The broadening of S where S is apparent, consistent with the separation of S into S_{ab} and S_{cd} in the presence of a D″ high velocity layer. Thus this method holds promise as an indicator of the existence of discontinuous high velocity layering in the deep mantle, which in past efforts has been predominantly probed using evidence for reflections between S and the core-reflected *ScS* (e.g. see review by Wysession *et al.* 1998); these are observed at much shorter epicentral distances, such as 60–80 deg. Therefore, a limitation in the *S–ScS* approach for detecting a discontinuity is geographical restrictions: large areas of the Pacific and Atlantic oceans result in larger epicentral distances between available earthquake-station paths. The significance of a D″ discontinuity detection probe at a different (larger) distance range is that new areas of the deep mantle may be probed.

3.3 Limitations and future work

In this study, we have chosen a Gaussian as PSF, which is arbitrary. Even though the results using a Gaussian seem to be good, there are undoubtedly better choices for the PSF. This is highlighted by some seismic pulses in the raw data appearing slightly asymmetrical

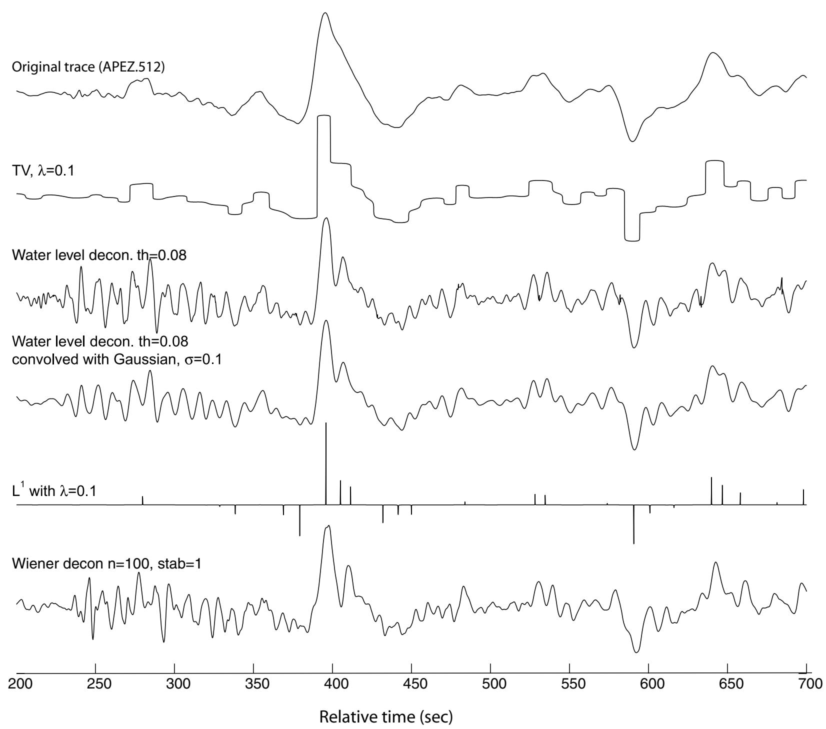

Figure 11. Original and deconvolved SV trace from a deep focus South American earthquake. The trace (104 deg. source receiver distance) contains *SKS* and *SPdKS*. As in the synthetic case a systematic broadening of *SKS* in the TV solution indicates the presence of the *SPdKS* phase.

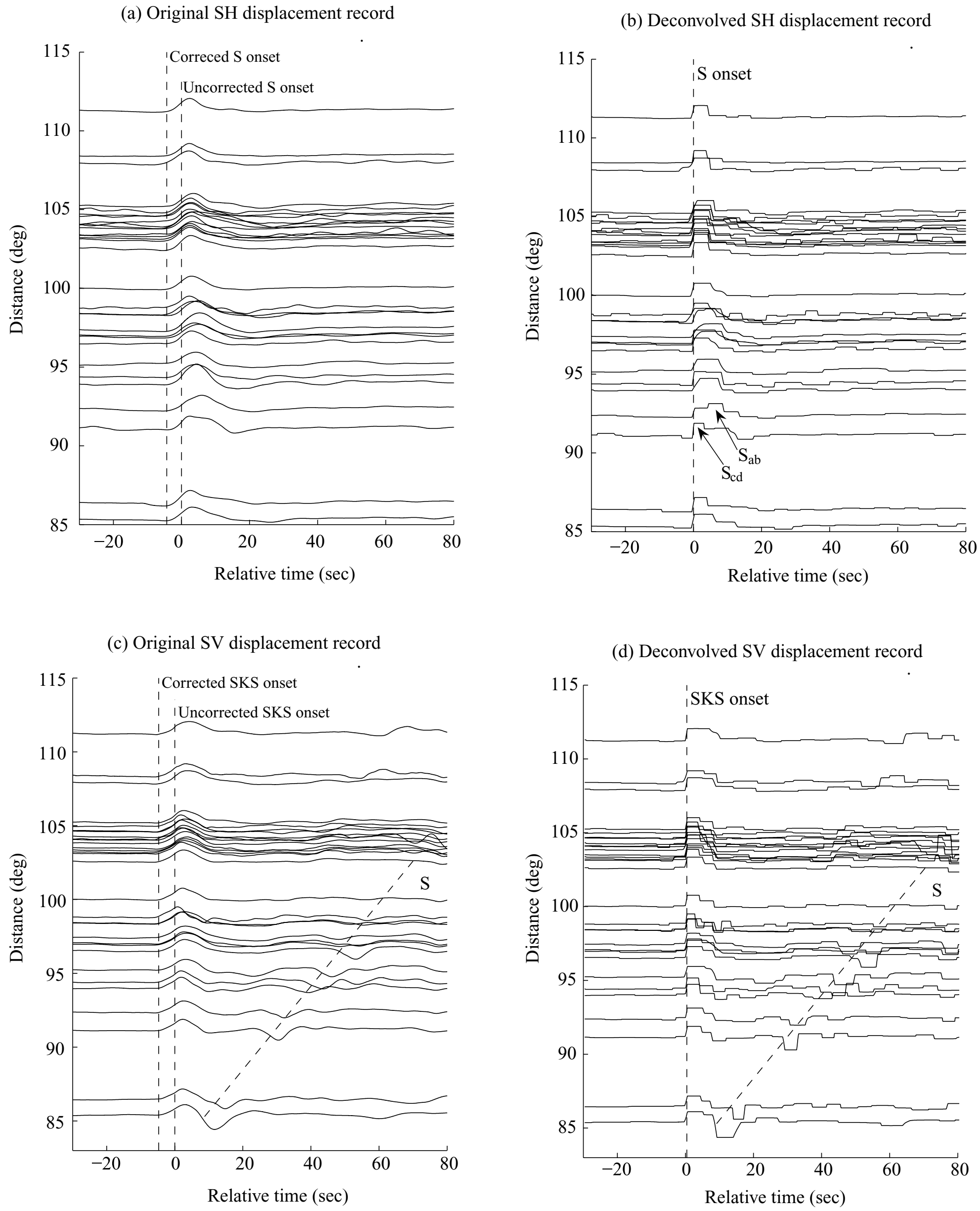

Figure 12. Original and deconvolved SH and SV recordings from a deep focus South American earthquake. Deconvolution was performed using a Gaussian PSF with $\sigma = 0.17$, sampled at 512 points between $-1/2$ and 1/2. The regularization parameter $\lambda = 0.1$ was chosen by the L-curve approach (Fig. 7). (a) Observed displacement SH traces. (b) Deconvolved SH traces. Records in (a) and (b) are aligned using times obtained from our edge detection approach on the deconvolved records in panel (b). Note that the deconvolved *S* pulses have approximately the same width less than 90 deg and greater than 103. Broadening between 90 and 98 deg is consistent with the presence of two D$''$ related phases: S_{ab} and S_{cd}, see also Fig. 13. (c) Observed and (d) deconvolved *SV* traces, where both panels are aligned using the edge-detected *SKS* times in panel (d).

(e.g. some of the *SKS* pulses in Fig. 12 possess a sharper upswing than the downswing), resulting in less sharp offsets in the deconvolved traces. A two-sided Gaussian, for example, could remedy this particular effect and will be pursued in future work. Alternative PSFs could also be derived directly by using a deconvolution method based on the data and an estimated source function, or by using more theoretical results of the filtering effect of the Earth's mantle. Future work will also include the application of the method to more events and different phases. In particular the robustness of the traveltime measurement must be further assessed and the potential to reveal structures in the signals that are not directly visible in the original signal due to the blurring has to be explored in more detail.

Here we have pursued an approach that has enabled improved differential analyses of phases that arrive closely in time. An inherent assumption is that the part of the signal removed in the reconstruction is common to all arrivals of interest. In fact, however, one arrival may experience enhanced attenuation relative to the other (such as *ScS*, relative to *S*, and so on). While this challenge is not new in deep Earth studies, especially those involving deconvolutions, we reiterate its potential presence for our method. However, the benefits of the TV-based deconvolution are clearly substantial, especially

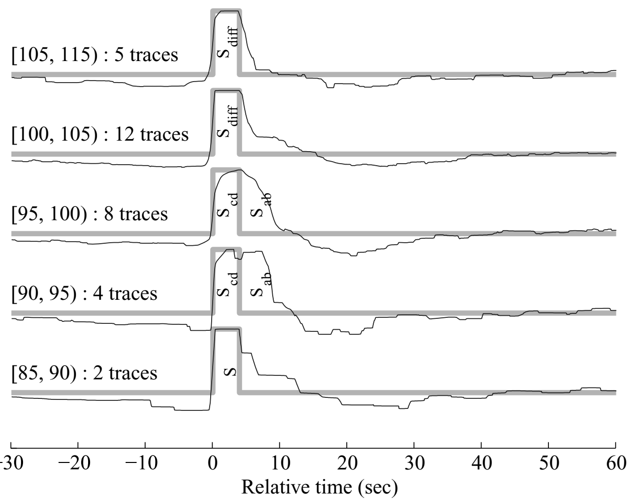

Figure 13. The deconvolved *SH* traces of Fig. 12 are grouped into distance bins then summed (thin solid lines). These overlie a thicker grey reference boxcar trace, that emphasizes the broadening of the *S* waves between around 90 and 100 deg, consistent with the presence of S_{ab} and S_{cd} phases due to a high velocity D″ layer.

the ability to make less ambiguous differential traveltime measurements.

4 CONCLUSIONS

We have presented a method to deconvolve PSFs from observed and synthetic seismograms to obtain more impulsive and narrower seismic signals, resulting in clearer visibility of more subtle waveform and timing variability in profiles of data. To accommodate the ill-posedness, that is, to control the noise amplification, we used TV regularization and described an efficient algorithm to compute the deconvolution. We showed that TV-regularized deconvolution results in sharp and clear reconstructions of both noise-free synthetic seismograms and noise-contaminated real seismograms of a test case. The signal reconstruction algorithm resulted in more accurate relative timing and amplitude information from the deconvolved traces than is presently possible with the raw traces. We have presented two example applications of the method: the closely arriving *SKS* and *SPdKS* waves, and the *S* and Sdiff waves the traverse the D layer. In each case, the reconstructed signals enable more accurate analysis and imaging of deep Earth structure.

ACKNOWLEDGMENTS

The authors wish to thank Sebastian Rost and Matthew Fouch for discussions and data, and two anonymous reviewers for constructive reviews that helped improve the manuscript. The work was supported in part by an NSF Collaboration in Mathematical and Geosciences grant CMG-02223.

REFERENCES

Andrews, H.C. & Hunt, B.R., 1977. *Digital Image Restoration,* Prentice-Hall, Inc., Englewood Cliffs, New Jersey, Prentice-Hall Signal Processing Series.

Bertero, M. & Boccacci, P., 1998. *Introduction to Inverse Problems in Imaging,* IOP Publishing Ltd., Bristol, UK.

Bijwaard, H., Spakman, W. & Engdahl, E.R., 1998. Closing the gap between regional and global traveltime tomography, *J. geophys. Res.,* **103,** 30 055–30 078.

Bracewell, R.N., 2003. *Fourier Analysis and Imaging,* Plenum Publishing Corporation, New York.

Castle, J.C. & van der Hilst, R.D., 2003. Using ScP precursors to search for mantle structures beneath 1800 km depth, *Geophys. Res. Lett.,* **30,** No. 8, 1422, doi:10.1029/2002GL016023.

Clearbout, J.F. & Muir, F., 1973. Robust modelling with erratic data, *Geopysics,* **38**(5), pp. 826–844.

Clearbout, J.F., 1985. *Imaging the Earth's Interior (IEI),* Blackwell Scientific Publications, Palo Alto, California.

Clayton, R.W. & Wiggins, R.A., 1976. Source shape estimation and deconvolution of teleseismic bodywaves, *Geophys. J. R. astr. Soc.,* **47,** 151–177.

Dahlen, F.A. & Tromp, J., 1997. *Theoretical Global Seismology*. Princeton University Press, Princeton, New Jersey.

Boschi, L. & Dziewonski, A.M., 2000. Whole Earth tomography from delay times of P, PcP, and PKP phases: lateral heterogeneities in the outer core or radial anisotropy in the mantle?, *J. Geophys. Res.,* **105,** 13 675–13 696.

Dodier, R., 1999. The RISO Project, http://riso.sourceforge.net/.

Dziewonski, A.M. & Anderson, D.L., Preliminary reference earth model, *Phys. Earth planet. Int.,* **25,** 297–356.

Garnero, E.J., 2000. Lower mantle heterogeneity, *Ann. Rev. Earth Planetary Sci.,* **28,** 509–537.

Grand, S.P., 2002. Mantle shear-wave tomography and the fate of subducted slabs, *Phil. Trans. R. Soc. Lond.,* A, **360,** 2475–2491.

Gu, Y.J., Dziewonski, A.M., Su, W. & Ekström, G., 2001. Models of the mantle shear velocity and discontinuities in the pattern of lateral heterogeneities, *J. geophys. Res.,* **106,** 11 169–11 199.

Hansen, P.C., 1994. Regularization tools: a Matlab package for analysis and solution of discrete ill-posed problems, *Numer. Alg.,* http://www.imm.dtu.dk/∼pch/Regutools/

Jonsson, E., Huang, S. & Chan, T.F., 1998. Total variation regularization in positron emission tomography, *Report 9848,* Department of Mathematics, UCLA, http://www.math.ucla.edu/applied/cam/index.html.

Kárason, H. & van der Hilst, R.D., 2001. Tomographic imaging of the lowermost mantle with differential times of refracted and diffracted core phases (PKP, P-diff), *J. geophys. Res.-Solid Earth,* **106**(B4), 6569–6587.

Katsaggelos, K.A., 1991. *Digital Image Restoration,* Springer-Verlag, Springer Series in Information Sciences, New York.

Keeling, S.L., 2002. Total Variation based convex filters for medical imaging, *Applied Mathematics and Computation,* Elsevier Science Inc., **139,** 101–119, New York.

Lay, T., Garnero, E.J. & Russell, S.A., 2004. Lateral variation of the D″ discontinuity beneath the Cocos Plate, *Geophys. Res. Lett.,* **31,** doi:10.1029/2004GL020300.

Margrave G.F., 2001. *Numerical Methods of Exploration Seismology with Algorithms in MATLAB,* Department of Geology and Geophysics, The University of Calgary, Canada.

Masters, G., Laske, G., Bolton, H. & Dziewonski, A.M., 2000. The relative behavior of shear velocity, bulk sound speed, and compressional velocity in the mantle: implications for chemical and thermal structure, in *Earth's Deep Interior: Mineral Physics and Tomography From the Atomic to the Global Scale,* pp. 63–87, eds Karato, S., Forte, A.M., Liebermann, R.C., Masters, G. & Stixrude, L., AGU, Washington, DC.

Moore, M.M., Garnero, E.J., Lay, T. & Williams Q., 2004. Shear wave splitting and waveform complexity for lowermost mantle structures with low-velocity lamellae and transverse isotropy, *J. geophys. Res.,* **109,** B02319, doi:10.1029/2003JB002546.

Müller, G., 1985. The reflectivity method: a tutorial, *J. Geophys.,* **58,** 153–174.

Ni, S., Tan, E., Gurnis, M. & Helmberger, D., 2002. Sharp sides to the African superplume, *Science,* **296,** 1850–1852.

Ni, S. & Helmberger, D.V., 2003. Ridge-like lower mantle structure beneath South Africa, *J. geophys. Res.,* **108**(B2), 2094, doi:10.1029/2001JB001545.

Nocedal, J. & Wright, S.J., 1999. *Numerical Optimization,* Springer-Verlag, New York.

Ring, W., 1999. Structural Properties of solutions of total variation regularization problems, preprint, http://www.uni-graz.at/imawww/ring/publist.html.

Ritsema, J. & van Heijst, H.J., 2000. Seismic imaging of structural heterogeneity in Earth's mantle: evidence for large-scale mantle flow, *Science Progress,* **83,** 243–259.

Rost, S. & Revenaugh, J., 2001. Seismic detection of rigid zones at the top of the core, *Science,* **294,** 1911–1914.

Rost S. & Thomas C., 2003. Array seismology: methods and applications, *Rev. Geophys.,* **40**(3), doi:10.1029/2000RG000100.

Rudin, L.I., Osher, S. & Fatemi, E., 1992. Nonlinear total variation based noise removal algorithms, *Physica D,* **60,** 259–268.

Stefan, W., Garnero, E. & Renaut, R., 2005. *Deconvolution Tools for Seismic Signals,* http://mathpost.la.asu.edu/∼stefan/seismodeconv.html

Strong, D.M. & Chan, T.F., 2000. *Edge-Preserving and Scale Dependent Properties of Total Variation Regularization,* Report 9848, Department of Mathematics, UCLA, http://www.math.ucla.edu/applied/cam/index.html.

Thorne, M.S. & E.J. Garnero, 2004. Inferences on ultralow-velocity zone structure from a global analysis of SPdKS waves, *J. geophys. Res.,* **109,** B08301, doi:10.1029/2004JB003010.

VanDecar, J.C., 1991. Upper mantle structure of the Cascadia subduction zone from non-linear teleseismic travel-time inversion, *PhD thesis*, University of Washington, Seattle.

Vogel, C.R. & Oman, M.E., 1996. Iterative methods for total variation denoising, *SIAM J. Sci. Statist. Comput.,* **17,** 227–238.

Vogel, C.R., 2002. *Computational Methods for Inverse Problems,* SIAM, Frontiers in Applied Mathematics.

Wysession, M., Lay, T., Revenaugh, J., Williams, Q., Garnero, E.J., Jeanloz, R. & Kellogg, L., 1998. The D″ discontinuity and its implications, in The Core-Mantle Boundary Region, 273–298, American Geophysical Union, Washington, DC.

Zhu, C., Byrd, R. Lu, P. & Nocedal, J., 1997. Software for large-scale bound-constrained or unconstrained optimization, http://www-fp.mcs.anl.gov/otc/Tools/LBFGS-B/.

Wysession, M.E., Langenhorst, A., Fouch, M.J., Fischer, K.M., Al-Eqabi, G.I., Shore, P.J. & Clarke, T.J., 1999. Lateral variations in compressional/shear velocities at the base of the mantle, *Science,* **284,** 120–125.